ADVANCED FUNCTIONAL MATERIALS
www.afm-journal.de

3D Printed Graphene Piezoresistive Microelectromechanical System Sensors to Explain the Ultrasensitive Wake Tracking of Wavy Seal Whiskers

Xingwen Zheng, Amar M. Kamat, Anastasiia O. Krushynska, Ming Cao, and Ajay Giri Prakash Kottapalli**

Many marine animals perform fascinating survival hydrodynamics and perceive their surroundings through optimally evolved sensory systems. For instance, phocid seal whiskers have undulations that allow them to resist noisy self-induced vortex-induced vibrations (VIV) while locking their vibration frequencies to wakes generated by swimming fishes. In this study, fully 3D-printed microelectromechanical systems (MEMS) sensors with high gauge factor graphene nanoplatelets piezoresistors are developed to explain the exquisite sensitivity of whisker-inspired structures to upstream wakes. The sensors are also used to measure natural frequencies of excised harbor (*Phoca vitulina*) and grey (*Halichoerus grypus*) seal whiskers and determine the effect of whisker orientation on the VIV, which can explain the possible natural orientation of whiskers during active hunting. Experimental investigations conducted in a recirculating water flume show that whisker-inspired sensors successfully sense an upstream wake located up to 10× the whisker diameter by locking to the frequency of the wake generator, thus mimicking the sensing mechanism of the seal whisker. The combination of VIV reduction and frequency-locking with the upstream wake generator demonstrates the whisker-inspired sensor's high signal-to-noise ratio, indicating its efficiency in long-distance wake sensing as well as its potential as an alternative to visual and acoustic sensors in underwater robots.

1. Introduction

In recent years, a variety of underwater robots,[1] including remotely operated vehicles (ROVs),[2] autonomous underwater vehicles (AUV),[3] and underwater bionic robots,[4] have been developed[5] and are widely used in sustainable development of marine economy,[6,7] underwater resource development,[8,9] and marine ecological protection.[10,11] Furthermore, the use of a swarm of underwater robots that sense their environment, communicate with each other, and coordinate behaviors to carry out underwater operations has gained popularity in recent years.[12,13] However, compared with the terrestrial environment, situational awareness in the underwater environment is rife with complications such as seawater corrosion, dim light, disturbed magnetic fields, complex terrain, and water flow disturbances. Due to the complexity of the underwater operating environment, the sensor systems-based environment detection and

X. Zheng, A. M. Kamat, A. G. P. Kottapalli
Advanced Production Engineering Group
Engineering and Technology Institute Groningen
Faculty of Science and Engineering
University of Groningen
9747AG Groningen, The Netherlands
E-mail: xingwen.zheng@rug.nl, zhengxingwen1993@gmail.com; a.g.p.kottapalli@rug.nl

X. Zheng, M. Cao
Discrete Technology and Production Automation Group
Engineering and Technology Institute Groningen
Faculty of Science and Engineering
University of Groningen
9747AG Groningen, The Netherlands

A. O. Krushynska
Computational Mechanical and Materials Engineering Group
Engineering and Technology Institute Groningen
Faculty of Science and Engineering
University of Groningen
9747AG Groningen, The Netherlands

A. G. P. Kottapalli
MIT Sea Grant College Program
Massachusetts Institute of Technology
77 Massachusetts, Avenue, Cambridge, MA 02139, USA

The ORCID identification number(s) for the author(s) of this article can be found under https://doi.org/10.1002/adfm.202207274.

DOI: 10.1002/adfm.202207274

information interaction among swarm robots are challenging problems. Although visual and acoustic sensors provide solutions, their performance is limited under complex terrain and low visibility conditions. Active sensing methods such as SONAR often suffer from poor resolution, and may also adversely affect the communication of marine animals. Optical methods, on the other hand, perform poorly in dirty and turbid water conditions.

In the marine world, we find examples of many animals that evolved impressive sensory systems heightening situational awareness—lateral line sensory system found in fishes can detect objects a few body lengths away,[14] electrical sensing of weakly electric fish can sense prey even in noisy conditions,[15,16] and ultrasensitive whiskers in seals have been shown to follow hydrodynamic trails left by fishes far away from the seal. The mechanotransduction sensors and sensing mechanisms in all of these species have evolved over millions of years to be perfectly adapted to their challenging surroundings. These sense organs play an essential role in local information perception and relative localization of fishes and seals with their neighbors, allowing the animals to perform impressive tasks such as schooling, escaping from predators, and foraging for prey in turbid underwater conditions. In recent years, several artificial electrical perception systems and artificial lateral line systems have been developed and applied to underwater target localization,[17,18] underwater object recognition,[19,20] and underwater robot control.[21,22] The artificial lateral line system composed of pressure sensor arrays and the artificial electrical perception system composed of alternating electrodes, have both been proven to operate successfully under complex terrain and dim light conditions, thereby improving the perception ability of underwater robots.

Seal whiskers have been the focus of recent studies due to their remarkable flow sensing that allows the seals to track the exact hydrodynamic trail of their prey.[23,24] The passive sensing system provides a promising design template for the development of flow sensors in underwater navigation, due to its low energy costs and truly long-distance sensing capabilities.[25] Phocid seals such as harbor (*Phoca vitulina*, **Figure 1**A) and grey (*Halichoerus grypus*, Figure 1B) seals possess whiskers with unique undulating geometries (Figure 1C) that are believed to play a crucial role in detecting the hydrodynamic stimuli generated from the wake of fish (Figure 1D) swimming far away.[25] The undulating whisker geometry is known to suppress noisy vortex-induced vibrations (VIV) generated downstream as the whisker is towed in flow during the forward swimming motion of the seal. When a high-aspect-ratio (HAR) cylindrical structure is subject to flow or is towed underwater, it vibrates due to the reaction generated by the shedding of the downstream vortices. Such a phenomenon is called vortex-induced vibration (VIV).[26] A HAR cylindrical structure allows the alternately shedding separated vortices to form a stable vortex street at the downstream area. In contrast, several studies[27–30] have shown that the undulating surface morphology (Figure 1C) of seal whiskers reduces primary vortex separations that gradually diffuse with the increasing downstream distances. As a result, undulating seal whiskers exhibit lesser VIV. While seal whiskers suppress VIV and remain still during the seal's forward motion (e.g., during hunting), they lock their vibration frequencies with those of the wakes of biologically relevant signals, generated for instance by an escaping prey.[23,24] Such vibrations are called wake-induced vibrations (WIV). In this manner, the seal whisker sensing system demonstrates a high signal-to-noise ratio (SNR) and exhibits high sensitivity to the hydrodynamic signals such as the vortex wake of escaping prey, allowing the seal to track these hydrodynamic trails accurately. The seal whisker's VIV suppression capability has also inspired the designs of flow sensors,[31–39] marine platforms,[40] underwater vehicles,[39,41] and aerofoils,[42] all of which featured undulating structural designs inspired by the seal whisker, and helped reduce self-generated noise and VIV-generated forces. Seal whisker inspired artificial flow sensor designs can mimic the sensing mechanisms deployed by the biological seal whiskers to attain ultrahigh sensitivity due to the high signal-to-noise ratio enabling long-distance wake detection and could provide promising alternatives to visual and acoustic sensors in detecting the surroundings of underwater robots.

In this work, we developed a fully 3D-printed piezoresistive MEMS flow sensor inspired by the long-distance wake detection capability of seal whiskers. The wake detection sensor was comprised of a seal whisker (real whiskers (Figure 1E) as well as 3D-printed whiskers constructed by a framework (Figure 1F) proposed by Hank et al.[27]) at the distal end of a 3D printed cantilever. Graphene nanoplatelets (GNP) dispersion was used as the high-gauge factor sensing nanomaterial at the proximal end of the cantilever to impart high sensitivity to the sensor. The whisker-inspired MEMS sensor was shown to function with high sensitivity to the wake signal, and a capacity to reject self-generated flow noise (VIV), thus explaining the sensing mechanism employed by seals in tracking wakes using their whiskers. Our three major contributions are listed below:

Natural frequency measurements of harbor and grey seal whiskers using 3D printed MEMS sensors—The natural frequencies of the excised harbor (*Phoca vitulina*, PV) and grey (*Halichoerus grypus*, HG) seal whiskers (Figure 1E) were measured using a 3D-printed piezoresistive MEMS cantilever sensor (**Figure 2**) and a high precision laser doppler vibrometer (LDV, **Figure 3**). While LDV measurements offer high precision, they are expensive and cannot be applied for high amplitude whisker vibrations. The 3D-printed piezoresistive MEMS sensor offers a low-cost alternative with a capacity to measure natural frequencies with a soft whisker embedding that mimics the follicle sinus complex (FSC)[43] at the base of the whisker. The FSC comprises soft tissue, muscular tissue and contains nerve fibers, and the reader is referred to publications that discuss the FSC microstructure of multiple seal species in greater detail (e.g., the habor seal,[43] the bearded seal,[44] and the northern elephant seal[45]). Due to their low form-factor, the MEMS whisker sensors also offer the benefit of being employed in real underwater wake detection and object detection experiments. The natural frequency of the whisker in water and whisker modal shapes, which could not be experimentally determined, were obtained using COMSOL Multiphysics simulations (**Figure 4**). Determination of the natural frequencies of the real seal whiskers and their correlation to the whisker geometry, material properties and the location on the muzzle is essential to understanding the exquisite sensitivity of the seal whisker enabled by the frequency lock-in mechanism as well as the possibility of different

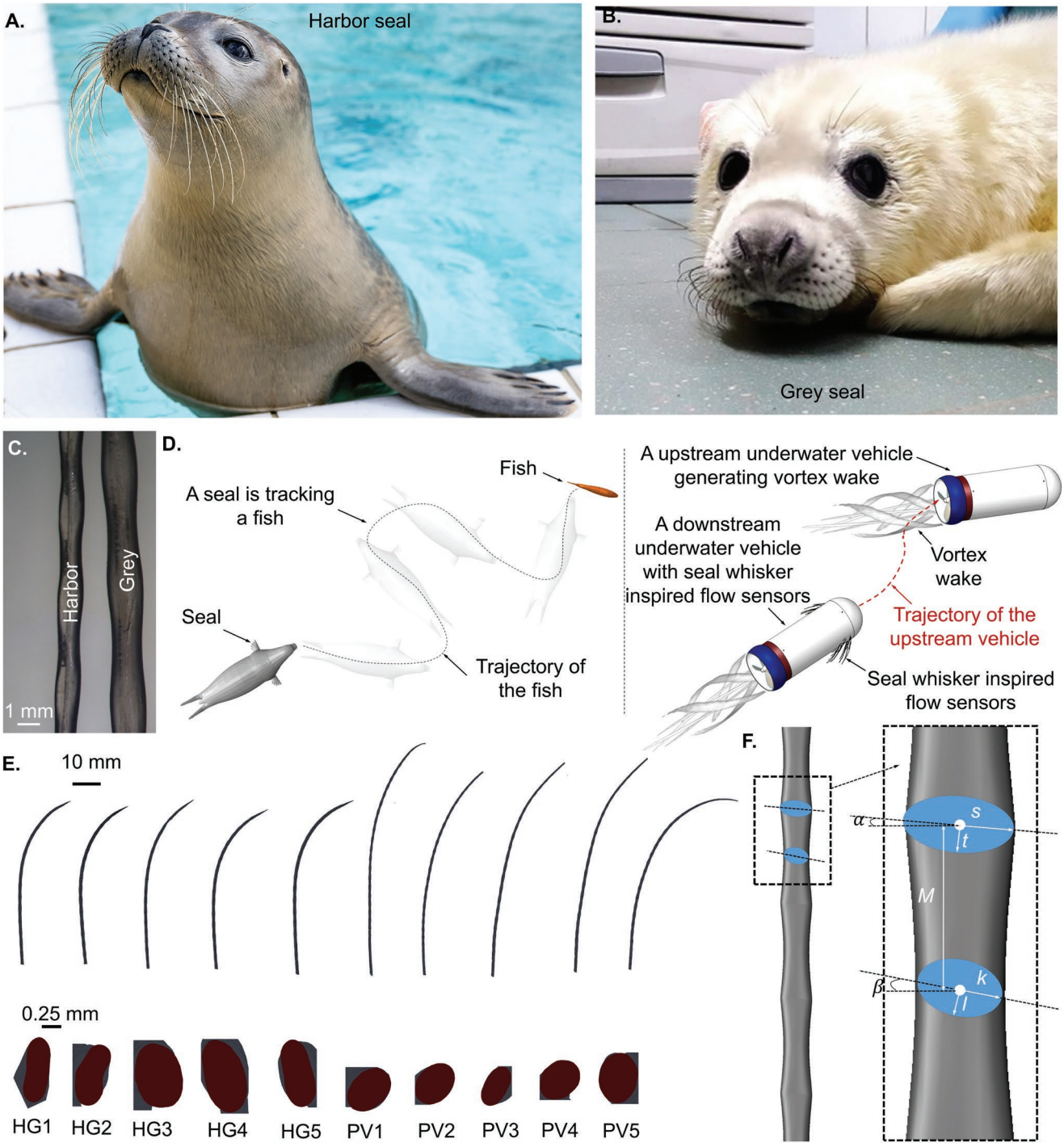

Figure 1. Seal and undulating seal whiskers. A) Harbor seal (*Phoca vitulina*), B) grey seal (*Halichoerus grypus*), and C) close-up images of their whiskers showing the unique undulating morphology. Seal images were provided by Zeehondencentrum, Pieterburen, The Netherlands, and reproduced with permission. D) A schematic sketch showing the ability of seal whiskers to track fish and the wake detection function of the seal whisker-inspired flow sensor on underwater vehicles. E) Five grey seal (*Halichoerus grypus*, HG) whiskers 1–5 and five harbor seal (*Phoca vitulina*, PV) whiskers 1–5 scanned using blue light scanning technology. Each scanned seal whisker was displayed in full length with a capture of the whisker base. All whiskers of the seals are shown with the same scale. F) The seal whisker structure constructed by the geometrical model proposed by Hank et al.[27]

whiskers responding to different frequency bands of hydrodynamic stimuli.

Understanding the correlation between VIV and whisker orientation using the 3D printed MEMS sensors—Through active motor control over the whiskers, seals can protract or relax their whiskers.[46] Previous wake tracking behavioral studies on harbor seals indicate that the whiskers are held erect during active wake tracking.[24] However, the orientation of the seal

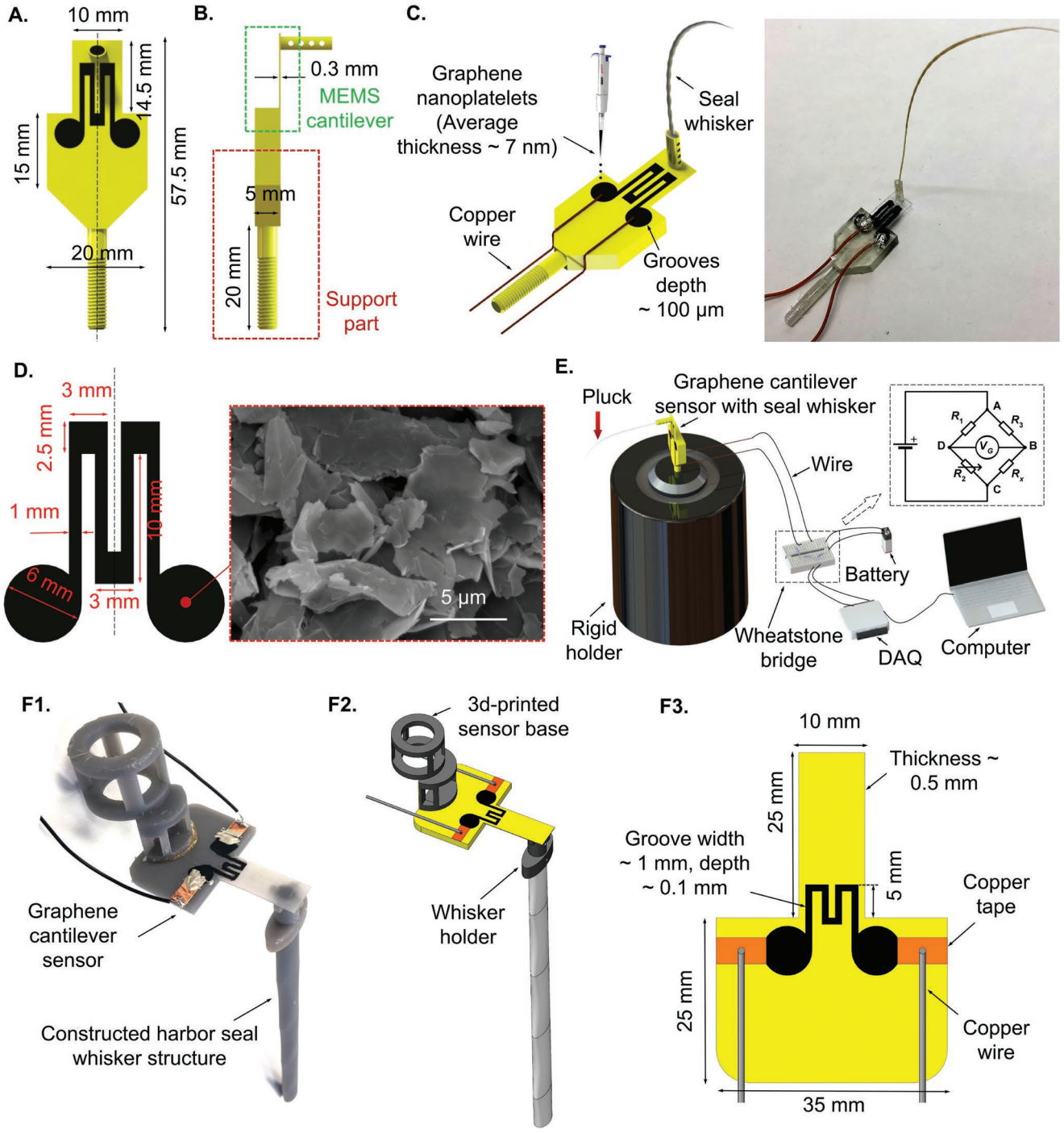

Figure 2. The cantilever graphene sensor. A,B) Dimensions of the sensor with a cantilever structure (aspect ratio ≈50, thickness ≈0.3 mm) used to measure the natural frequency. C) Conductive graphene nanoplatelets (GNP) in ink-drop casting and prototype cantilever sensor with a seal whisker. D) Dimensions of the GNP stain gauge and the scanning electron (SE) micrograph of graphene nanoplatelets in microchannels (depth ≈100 µm). E) A schematic sketch showing experimental setups of cantilever sensor-based natural frequency measurements. The F1) prototype and F2) CAD model of the graphene cantilever sensor used for WIV and VIV measurements of seal whiskers. The 3d-printed sensor was attached to a 3d-printed sensor base using the hot-melt adhesive. Next, the 3d-printed seal whisker structure was inserted into a 3d-printed whisker holder, which was attached to the end of the 3d-printed sensor. F3) Dimensions of the cantilever sensor.

whiskers in the wake during active hunting is unknown so far as it is difficult to quantify experimentally. In this work, using the 3D printed piezoresistive MEMS sensors and conducting recirculating water flume experiments (Figure 3), we identified the effect of orientation of the whisker with respect to the oncoming flow (angle of attack) on the VIV response of the

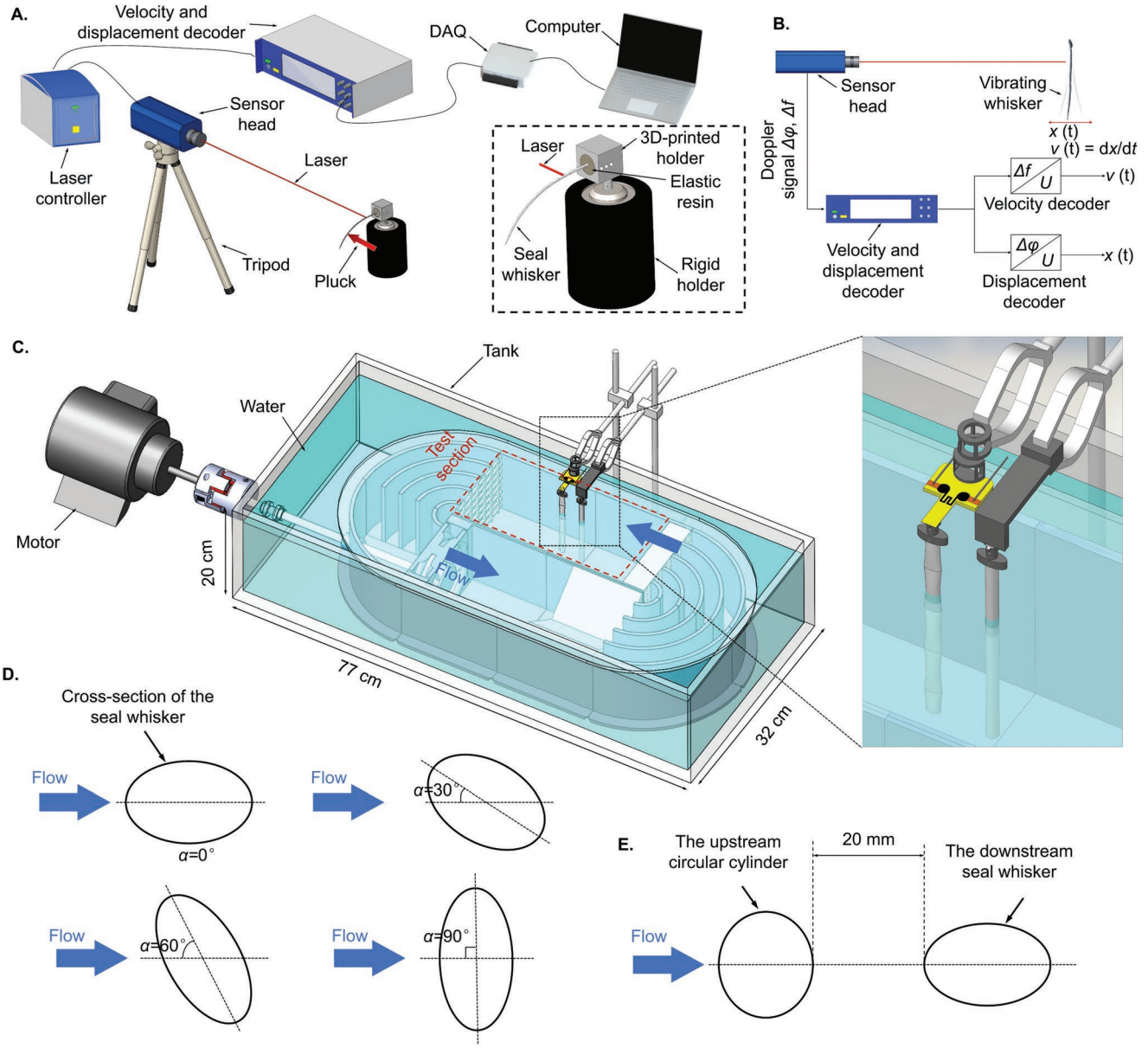

Figure 3. The LDV system and the recirculating water flume. A) A schematic sketch showing LDV-based measurements of seal whiskers. B) The operating principle of the LDV system. C) The recirculating water flume used to conduct VIV and WIV measurements of seal whiskers. D) Angles of attack of seal whiskers in VIV measurements. E) The upstream circular cylinder and the downstream seal whisker in WIV measurements.

whisker to hypothesize the possible natural orientation of the whiskers during active tracking that would benefit the most from reduced VIV and drag force.

Wake detection ability of the 3D printed whisker inspired MEMS sensor at long distances—Whisker-inspired structures mounted at the distal tip of 3D-printed piezoresistive MEMS cantilevers were employed to further explain the wake sensing capability of the whisker structures. The whiskers were observed to lock their vibration frequency with the wake-induced vibration (WIV) frequency of the oncoming wake while simultaneously minimizing the self-induced VIV. A comparative analysis of cylindrical structures and whisker-inspired structures, mounted on MEMS sensors and tested in steady flows in the presence of a wake generator in recirculating water flume (Figure 3), provides further understanding regarding how seal whiskers detect minute wake streets generated by fishes far away as the seals themselves swim at high speeds.

2. Results and Discussion

2.1. MEMS Sensor and LDV Aided Natural Frequency Measurements of Real Seal Whiskers

The natural frequencies of five real harbor (*Phoca vitulina*, PV1-PV5) and grey (*Halichoerus grypus*, HG1-HG5) seal

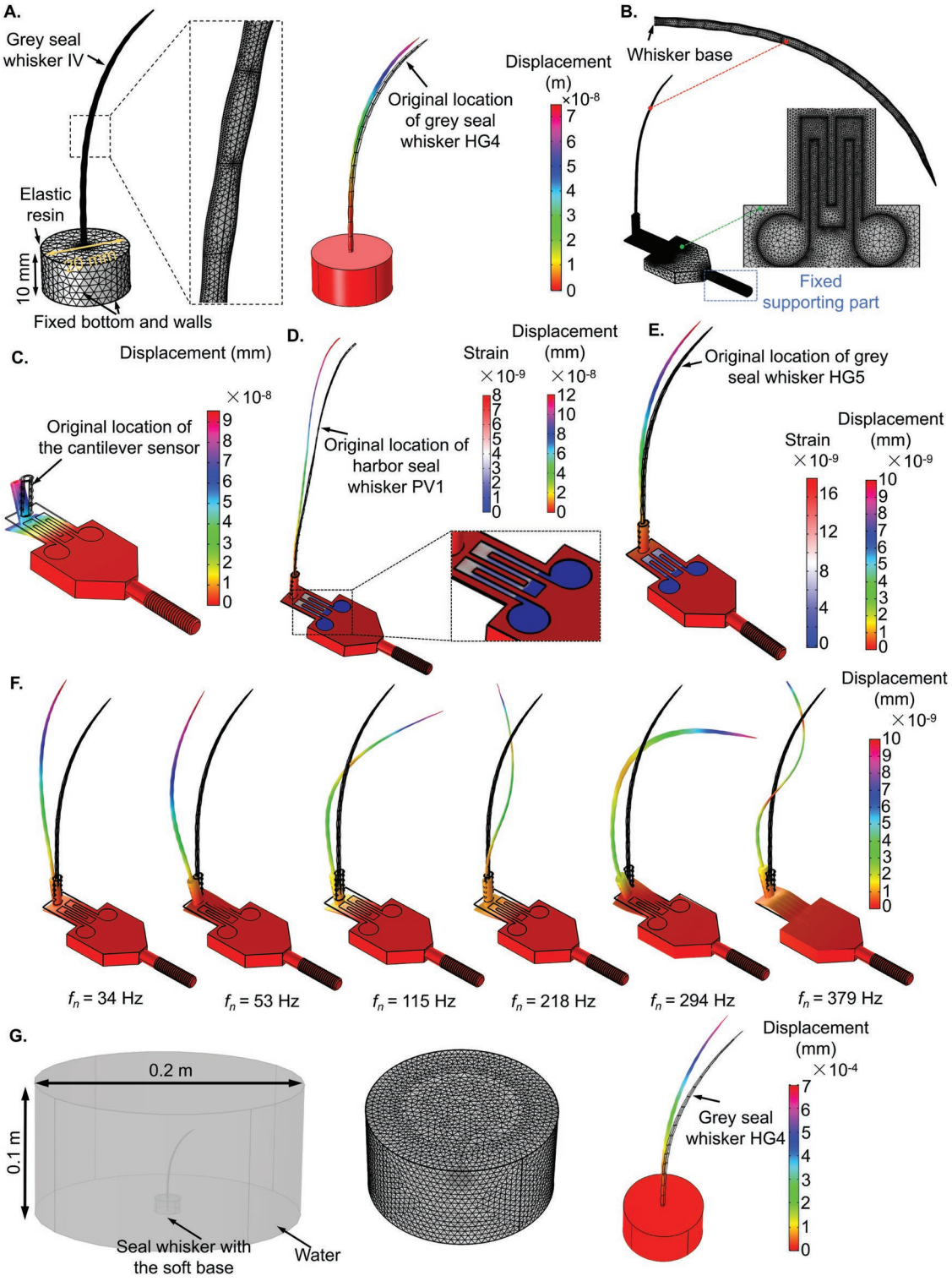

Figure 4. COMSOL Multiphysics-based natural frequency simulations of the printed cantilever sensor and seal whiskers. A) The generated mesh and the first mode shape (deformation factor: 50 000) of the isolate grey seal whisker IV with and without a soft base. B) The generated mesh of the cantilever sensor with the seal whisker. C) The first mode shape (deformation factor: 50 000) of the printed sensor (natural frequency ≈132 Hz). The first mode shape (deformation factor: 50 000) of the cantilever sensor with D) Harbor seal whisker I (PV1, natural frequency ≈34 Hz) and E) Grey seal whisker V (HG5, natural frequency ≈34 Hz). F) Various mode shapes (deformation factor: 200 000) of Grey seal whisker V (HG5). G) Calculation domains of simulations, in which the seal whisker with the soft base was located in a cylindrical water domain and the first mode shape of Grey seal whisker IV (deformation factor: 10).

whiskers (Details: Experimental Section) were measured using MEMS cantilever sensors as well as using the LDV system. In both cases, each of the whiskers was individually mounted and plucked (see Experimental Section). The plucking act conducted on the seal whisker resulted in a significant variation of the time-series outputs generated by the piezoresistive sensing element of the MEMS cantilever sensor and the LDV sensor, which gradually decreased when the seal whisker's vibration eventually damped down to zero (**Figure 5**A,B; also see the Video S1, Supporting Information). In both these experiments,

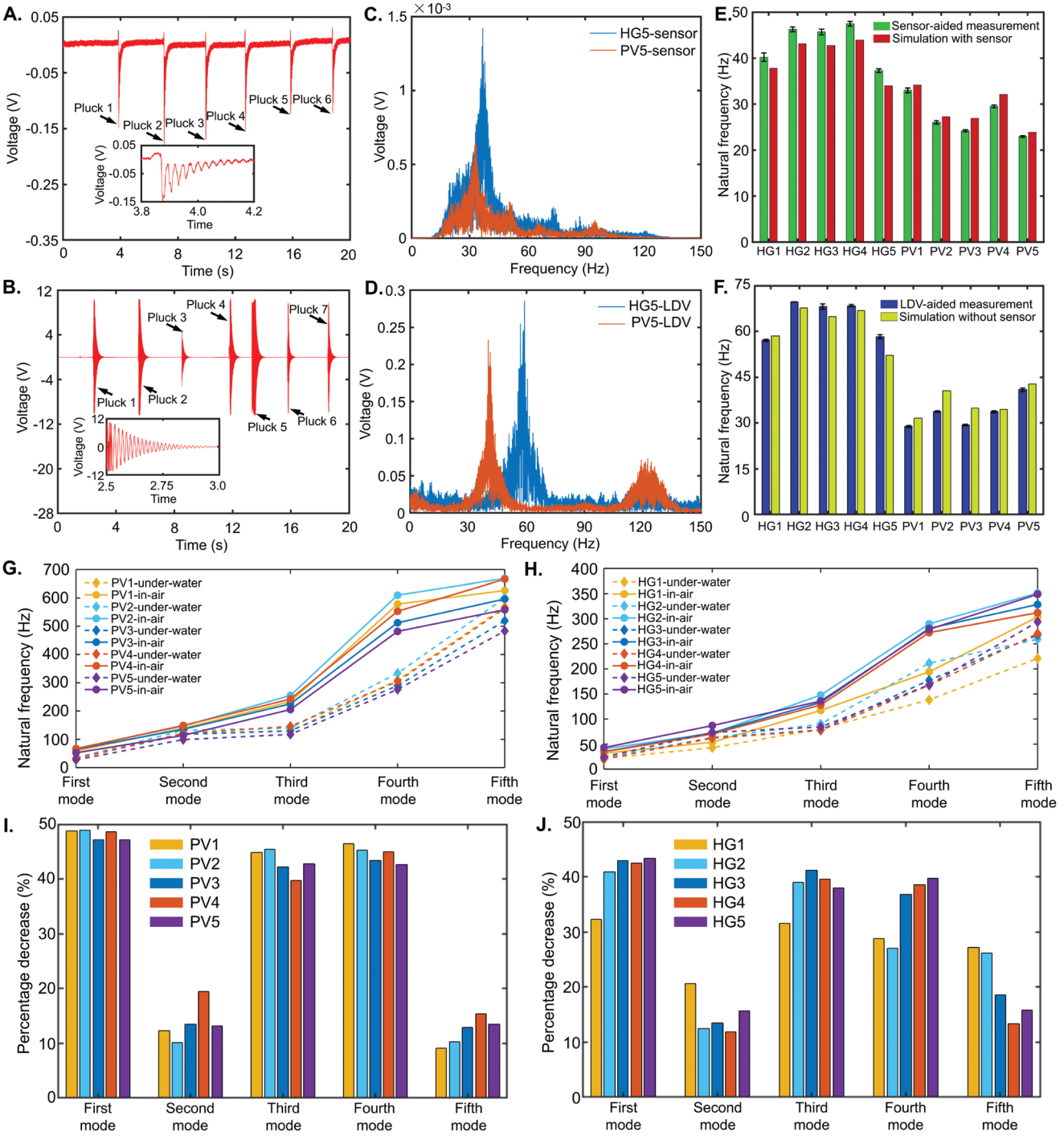

Figure 5. Measured and simulated natural frequencies. Time series of A) the cantilever sensor and the B) LDV data when the seal whisker was plucked. The FFT analysis on the time-series of C) the cantilever sensor and the D) LDV data. Comparisons between the simulated and measured natural frequencies in E) cantilever sensor and F) LDV-based measurements. Various modes of natural frequencies under the water (dotted line) and in the air (solid line) for G) harbor (PV) and H) grey seal (HG) whiskers. The percentage decrease of the natural frequency under the water compared to that in the air for I) harbor (PV) and J) grey seal (HG) whiskers.

Table 1. Simulated and measured natural frequencies (first mode) in cantilever sensor and LDV-based measurements.

Seal whiskers	Length [mm]	Average thickness [mm]	Sensor-aided measurement [Hz]	Simulation of the cantilever sensor with the seal whisker [Hz]	Difference between simulations and cantilever sensor-based measurements [Hz]	LDV-aided measurement [Hz]	Simulation of isolate seal whisker with soft base [Hz]	Difference between simulations and LDV-based measurements [Hz]
HG1	69.20	0.3967	40	38	2	57	59	2
HG2	66.70	0.3833	46	43	3	70	68	2
HG3	69.83	0.3967	46	43	3	68	65	3
HG4	68.54	0.39	48	44	4	68	67	1
HG5	75.67	0.4267	37	34	3	58	52	6
PV1	96.85	0.4333	23	24	1	29	32	3
PV2	84.06	0.44	30	32	2	34	40	6
PV3	89.44	0.4267	24	27	3	29	35	6
PV4	92.01	0.39	26	27	1	34	35	1
PV5	72.20	0.3833	33	34	1	41	43	2

the natural frequencies of the seal whiskers were measured by conducting FFT on the time series data and noting the dominant peaks in the frequency domain (Figure 5C–F). Due to the low-frequency noise generated during the plucking action, a high-pass filter was applied to the time series of the cantilever sensor's outputs to remove the frequency components less than 10 Hz.

The simulations (Details: Experimental Section) showed that the isolated cantilever sensor's natural frequency (without the whisker) was ≈132 Hz, Figure 4C, which was much higher than that (23–48 Hz) of the whisker-on-cantilever system (Figure 4D,E), indicating that the cantilever's natural frequency will not be excited by the seal whisker when it was plucked. As a result, the cantilever sensor could efficiently measure the natural frequency of the plucked seal whisker. In addition, the FEM simulations also enabled us to obtain the whisker mode shapes at a band of natural frequencies (Figure 4F).

We compared simulated and measured results of the first-mode natural frequencies for the whisker-on-sensor system (Figure 5E,F). The cantilever sensor-measured and simulated natural frequencies agreed well (with errors ≈1–2 Hz for harbor seal whiskers and 2–4 Hz for grey seal whiskers, Figure 5E and **Table 1**), validating the results of the cantilever sensor-based measurements. Besides, discrepancies between the LDV-measured and simulated natural frequencies were ≈1–6 Hz for grey seal whiskers and ≈1–7 Hz for grey seal whiskers (Figure 5F and Table 1). The measurements showed that grey seal whiskers had higher natural frequencies (43 ± 4 Hz in the cantilever sensor-based measurements and 64 ± 6 Hz in the LDV-based measurements) than harbor seal whiskers (27 ± 4 Hz in the cantilever sensor-based measurements and 33 ± 5 Hz in the LDV-based measurements). The natural frequency f_n of a uniform rectangular cantilever (length = L, thickness = t, Young's modulus = E, and density ρ) can be estimated as: $f_n = 1.94 \frac{t}{L^2}\sqrt{\frac{E}{\rho}}$,[47] which indicates that the natural frequency decreases with the cantilever length. In line with this, the above differences in natural frequencies between harbor and grey seal whiskers may be caused by the shorter length of the selected grey seal whiskers (Figure 1E).

As mentioned above, the cantilever sensor's first-mode natural frequency was ≈3–6 times higher than that of the seal whisker on it; hence, the variation of the cantilever sensor's output was mainly due to the vibration of the seal whisker. However, using the cantilever sensor, it is difficult to isolate the natural frequency of the seal whisker alone as the measured natural frequency is a function of the cantilever-and-whisker system and not that of an isolated seal whisker alone. Therefore, we also conducted LDV measurements to investigate the natural frequency of isolated whiskers and ensure that the measurements are from a soft mounting of the whisker, as is in the case of real seal whiskers embedded into FSC. The aforementioned variations in the experimental set-ups caused the differences in the natural frequency measurements conducted using the cantilever sensor and LDV system. A careful inspection revealed that the agreement between methods-based measurements was better for harbor than grey seal whiskers (difference ≈4–8 Hz for harbor and 17–23 Hz for grey seal whiskers). This could be because the measured natural frequency of the isolated grey seal whiskers (≈64 ± 6 Hz measured by LDV) was closer to the natural frequency of the isolated cantilever sensor (≈132 Hz). In contrast, the frequency of the isolated harbor seal whiskers (≈33 ± 5 Hz measured by LDV) was farther away from that of the cantilever sensor. This indicated that the cantilever sensor could be a good substitute for the much more expensive LDV method for cases where the whisker's natural frequency is ≈3–6× smaller than the cantilever itself. In addition, the above high accuracy of the cantilever sensor in measuring the natural frequency of milliliter-scale seal whisker provided the first way to validate the sensor operation.

Previous work[48,49] mainly focused on the seal whisker's first-mode natural frequencies, which were the lowest frequencies at which deformations occurred. Though the first mode of natural frequency is easiest to be excited by the external stimuli, investigating more modes of natural frequencies can contribute to determining the seal whisker's detectable frequency components, which are usually encoded with a range in the surrounding under disturbances. For example, the wake of fish and other prey of seals varied from <10 Hz to >100 Hz.[50] Besides, while most of the existing works in the literature[51,52]

mainly focused on the vibrating frequencies of seal whiskers caused by a specific flow condition, insufficient attention was paid to the seal whisker's own natural frequency underwater. Considering that the seal whisker's vibrating frequency under the water could be affected by the flow passed by[51,52] and the surrounding hydrodynamic stimuli with various frequency components,[28,53–55] therefore measuring underwater natural frequencies of seal whiskers can determine the frequency range within which various seal whiskers vibrated most. Furthermore, all of the works in the literature conducted the natural frequency measurements in the air (natural frequencies underwater would be lower).[56] As a result, the measured or simulated natural frequencies were not completely convincing when explaining the frequency synchronization of the seal whisker with the hydrodynamic stimuli. To address the above limitations in previous works, we compared various modes of natural frequencies in the air and under the water in this article.

Because of the damping caused by the dense water medium, the vibration intensities of seal whiskers were significantly reduced and were insufficient to excite the cantilever sensor. Besides, the refraction and reflection of the laser under the water made it difficult to measure the natural frequencies of seal whiskers under the water using the LDV system. As a result, COMSOL multiphysics-based simulations were used to simulate the seal whiskers' natural frequencies under the water and were compared to the simulated results of in-air natural frequencies (Figure 5G,H and **Table 2**). It was observed that smaller natural frequencies ($f_{n_{water}}$ and $f_{n_{air}}$) were observed in harbor seal whiskers at every mode of shape compared with grey seal whiskers (Figure 5G,H). Besides, the first five modes of natural frequencies of seal whisker decreased by 9%–49% in underwater conditions (Figure 5I,J and Table 2). In addition, the second mode of natural frequencies decreased least (10%–21%, Figure 5I,J and Table 2)

Table 2. Various modes of natural frequencies under the water and in the air.

Seal whiskers	Conditions	First mode/Hz	Second mode/Hz	Third mode/Hz	Fourth mode/Hz	Fifth mode/Hz
HG1	Under the water	30	122	129	310	569
	In the air	59	139	233	579	626
	Percentage decrease	49.15%	12.23%	44.64%	46.46%	**9.11%**
HG2	Under the water	35	132	140	334	600
	In the air	68	147	255	610	669
	Percentage decrease	48.53%	10.20%	45.10%	45.25%	10.31%
HG3	Under the water	34	117	130	290	519
	In the air	65	136	225	512	596
	Percentage decrease	47.69%	13.97%	42.22%	43.36%	12.92%
HG4	Under the water	34	120	146	305	564
	In the air	67	149	242	553	666
	Percentage decrease	**49.25%**	19.46%	39.67%	44.85%	15.32%
HG5	Under the water	28	99	118	277	483
	In the air	52	114	205	482	559
	Percentage decrease	46.15%	13.16%	42.44%	42.53%	13.60%
PV1	Under the water	21	43	80	138	221
	In the air	32	54	117	194	304
	Percentage decrease	34.38%	20.37%	.31.62%	28.87%	27.30%
PV2	Under the water	24	63	90	211	259
	In the air	40	71	148	290	351
	Percentage decrease	40%	11.27%	39.19	27.24%	26.21%
PV3	Under the water	20	63	78	178	267
	In the air	35	72	133	281	329
	Percentage decrease	42.86%	12.50%	41.35%	36.65%	18.84%
PV4	Under the water	20	62	77	167	271
	In the air	35	70	128	272	312
	Percentage decrease	42.86%	11.43%	39.84%	38.60%	13.14%
PV5	Under the water	24	73	84	168	294
	In the air	43	87	136	279	349
	Percentage decrease	44.19%	16.09%	38.24%	39.78%	15.76%

*The biggest and smallest percentage decreases are marked in bold.

underwater compared to other modes of natural frequencies for all seal whiskers.

Prior research in literature[24,52,57,58] suggested that the seal whisker can amplify hydrodynamic signals (e.g., dominant vortical frequencies in a wake) around its natural frequency by resonance, thus enabling the seal's detection of the hydrodynamic stimuli. In addition, seal whisker arrays with various whisker lengths and thicknesses have different natural frequencies, enabling the seal to encode a band of frequency of the hydrodynamic stimuli. The LDV measurements and the simulated results underwater, which were more similar to the actual scenario that the whiskers are embedded in a soft tissue comprising the follicle-sinus complex (FSC),[43] can provide more insights into the biological mechanism of the seal whisker's sensing to underwater disturbances with various frequency components. Values of the first five modes of $f_{n_{water}}$ were ≈28–600 Hz for harbor seal whiskers and ≈20–294 Hz for grey seal whiskers, indicating a capability of sensing in a broad range of frequency components encoded in underwater disturbances such as the wake (varied from <10 Hz to >100 Hz) of fish and other prey.

2.2. Investigation of VIVs at Various Angles of Attacks

When located in an oncoming flow, the angle between the flow direction and the major radius of the seal whisker is defined as the angle of attack (AOA) of the seal whisker. When the major radius of the seal whisker is parallel to the flow direction, the AOA equals zero. Furthermore, the AOA = 0° would be the preferred orientation when swimming since this exposes the smallest frontal area of the seal whisker to the flow, ensuring the lowest drag on the seal whisker. However, the AOA can change as the seal moves its head and orients itself to the flow. Murphy et al.[46] studied the VIV response of harbor seal, elephant seal, and California sea lion whiskers with various AOA values in the flow. However, only three AOA values, including 0, 45, and 90°, were explored without a comprehensive investigation of VIV responses across a considerable range of AOA. As a result, it is essential to explore how the VIV response of the seal whisker changes with its varying orientation to the flow.

We investigated the VIV response of the seal whisker at various AOAs through COMSOL Multiphysics-based simulations and 3D printed MEMS sensor-aided recirculating water flume experiments. In the experiments, due to the difficulty in measuring the tiny vibrations generated by the real-scale (millimeter-scale) seal whisker, we first constructed a harbor seal whisker using the geometric model (Figure 1F) proposed by Hanke et al.,[27] then we scaled it up ten times (Details: Experimental Section). Then, it was attached to the distal tip of a 3D-printed cantilever sensor (Details: Experimental Section). Finally, the recirculating water flume experiments (Details: Experimental Section; Video S2, Supporting Information) were conducted to measure the VIVs of the constructed seal whisker structure with various AOAs.

In simulations, two cases were investigated: 1) Simulating the shedding vortices distributions behind an elliptical cross-section of the seal whisker, which had various AOAs (0, 30, 60, and 90°; Video S3, Supporting Information), and 2) Simulating the WIVs of one isolated circular cylinder and one isolated seal whisker in the presence of an upstream circular cylinder (Video S4, Supporting Information). In the simulations, a no-slip wall condition and a free tetrahedral mesh with $\approx 10^4$ elements were applied to the calculation domains. Case 1 simulated the experiments of measuring VIV of seal whisker structure with various AOAs, while Case 2 simulated the WIV measurements. The flow velocity was set as 0.15 m s^{-1} in Case 1 and Case 2 to match the actual flow velocity ranges in the corresponding measurements.

In simulations, an elliptical cross-section of the seal whisker structure was located with various AOAs in the oncoming flow. It was observed (**Figure 6**A) that the flow vorticity intensity, which was characterized by the vorticity magnitude fluctuations and the distribution area of shedding vortices, showed an increasing trend when the AOA of the seal whisker increased from 0° (major radius parallel to the flow) to 90° (minor radius parallel to the flow). Such a flow vorticity trend caused the VIV in experiments (Figure 6B; Video S5, Supporting Information) to increase from AOA = 0° (major radius parallel to the flow) to AOA = 90° (minor radius parallel to the flow), which matched Murphy et al.'s[46] experiments of investigating VIV response of harbor seal, elephant seal and California sea lion whiskers with AOA of 0, 45, and 90°. Besides, VIV-AOA regularity exhibited symmetrical distribution around AOA = 90°. The above characteristics indicated that the AOA = 90° orientation is probably not physically realistic because the seal whisker serves as a bluff body and loses the advantage of a streamlined elliptical shape which is the case at the AOA = 0° orientation. This suggested that the seal whisker may keep its major radius parallel to the flow when the seal is swimming, ensuring the smallest self-generated noise caused by the VIV and thus realizing the most sensitivity to the underwater disturbances. Furthermore, the VIV had a sharp increase when the AOA exceeded 30° and a sharp decrease when the AOA exceeded 150°, indicating that AOA = 0°–30° or 150°–180° was a range where the advantages of VIV reduction due to undulations hold true. The limits measured using our sensors matched the angle limit determined by Wang & Liu,[59] thus validating the performance of our sensor.

2.3. Long-Distance Wake Detection

The mechanism governing how the seal whisker vibrates in fish wake-like vortices and exhibits ultrasensitive trail tracking ability to fish trail is an open question. Beem & Triantafyllou[28] proposed a mechanistic explanation that the WIV response of undulating seal whiskers resulted from its 'slaloming' movement through which the whisker efficiently extracts energy from an upstream vortex generator. Specifically, the seal whisker structure was first pulled to the closest oncoming vortex on one side because of the low-pressure area associated with the vortex. Then it was pulled to the other side as the wake shed by the upstream circular cylinder progressed forward. To further explain how the seal whisker interacts with fish wake-like vortices in an oncoming flow and to provide a mechanistic explanation for the ultrasensitive fish trail tracking ability of the seal whisker, we conducted WIV measurements using a 3D-printed seal whisker structure (scaling ten times up the actual dimensions

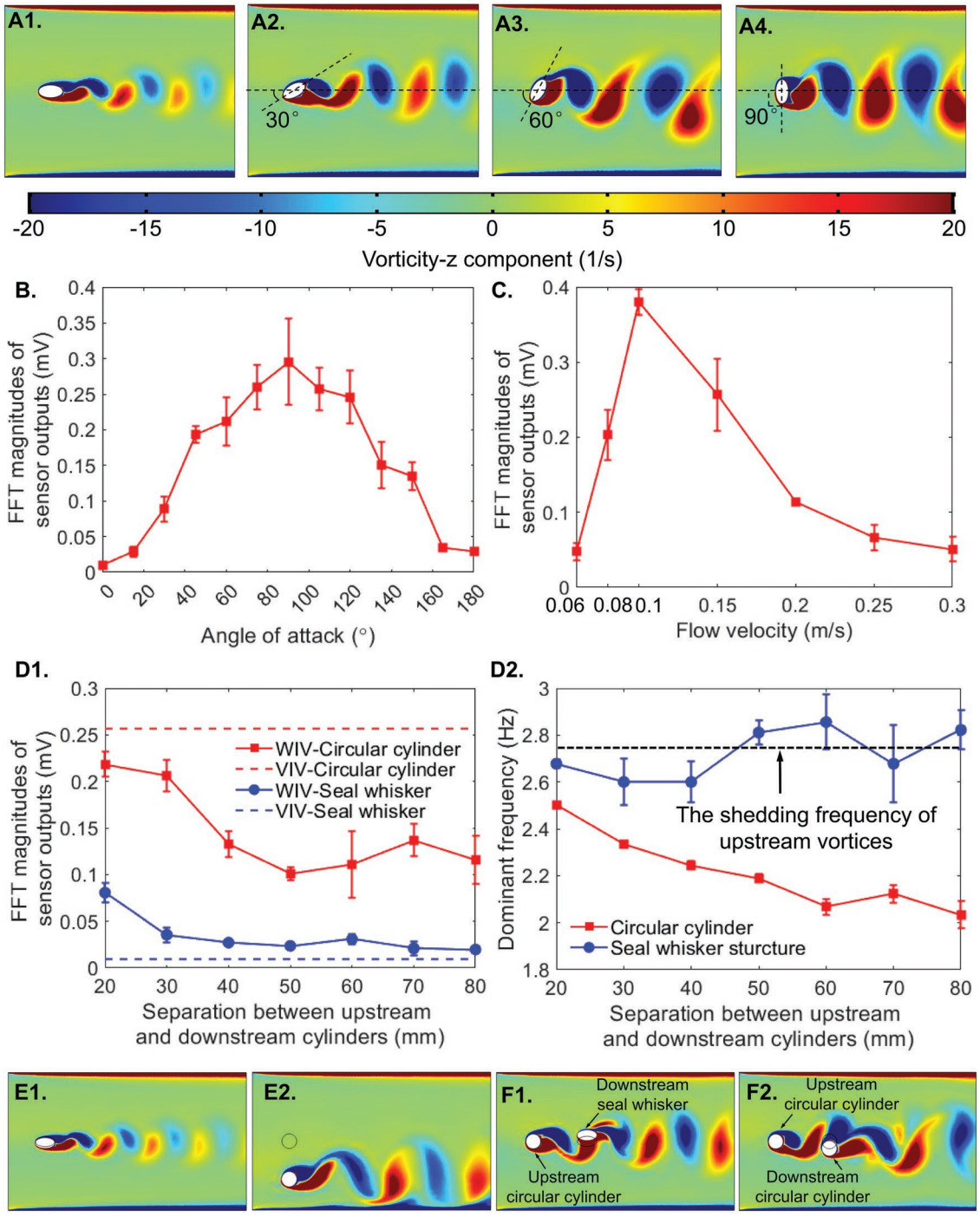

Figure 6. Simulated and experimental results. The vorticity distributions in shedding vortices of the seal whisker (shown by its elliptical cross-section) when it was located with an AOA of A1) 0, A2) 30°, A3) 60°, and A4) 90°. The oncoming flow was from left to right. Animations of the shedding vortices are presented in Video S3 (Supporting Information). B) Cantilever sensor-measured VIVs with various AOAs of the seal whisker. C) The VIV of the circular cylinder with various flow velocities. D1) Cantilever sensor-measured WIVs of the seal whisker and D2) dominant frequencies with various separations between the upstream circular cylinder and the downstream seal whisker structure (natural frequency ≈53.8 Hz). E) COMSOL Multiphysics-based simulations of the VIVs of E1) the seal whisker and E2) the circular cylinder. F) COMSOL Multiphysics-based simulations of the WIVs of F1) the seal whisker and F2) the circular cylinder. Animations of VIV and VIV simulations are presented in Video S4 (Supporting Information).

of a real seal whisker) with various separations from the upstream wake generator, which was a 3D-printed circular cylinder (see Experimental Section).

The vibrations of the downstream seal whisker were characterized by the dominant peaks in the frequency domain of the FFT analyses on the time series of the sensor to which the

downstream seal whisker was attached. Before conducting the experiments, we measured the VIVs of the isolated circular cylinder at various flow velocities (0.06–0.3 m s^{-1}). The Reynolds number,[60] which characterized the flow patterns in different fluid flow situations, increased from ≈480 to ≈2400 with the increasing flow velocity (0.06–0.3 m s^{-1}). The flow varied with the increasing Reynolds numbers, causing the varied shedding vortices intensity and vortices-induced reaction on the circular cylinder, and finally resulting in the varied VIV of the circular cylinder with the flow velocity. It was observed that the VIV of the circular cylinder increased and then decreased with the flow velocity (Figure 6C). The VIV reached a peak when the flow velocity was 0.1 m s^{-1} (Reynolds number ≈800), indicating that the reaction generated by the shedding vortices, and reversely, and the shedding vortices intensity of the circular cylinder was biggest at 0.1 m s^{-1}. As a result, the oncoming flow velocity was fixed at 0.1 m s^{-1} to ensure sufficient distributions downstream when investigating WIVs of the downstream seal whisker/circular cylinder with various upstream–downstream separations. In this work, we compared the WIVs of the seal whisker structure and circular cylinder with similar dimensions (diameter 8 mm). When the seal whisker structure was located in an oncoming flow without an upstream vortex generator, the cantilever sensor recorded minimal vibrations of the seal whisker structure compared to the circular cylinder due to the VIV suppression of the seal whisker (Figure 6D1). However, in the presence of an upstream wake generator, the seal whisker structure's vibrations (WIVs) were 2–10× more than its VIV when it was located in the shedding vortices, indicating an efficient response to long-distance stimuli. Besides, the WIVs increased with the decreasing upstream–downstream separations. Finally, the dominant frequency of the WIVs nearly kept constant and locked to the vortex-shedding frequency (≈2.75 Hz) of the upstream circular cylinder for a considerable upstream—downstream separation varying from 20 mm (2.5× the whisker diameter) to 80 mm (10× the whisker diameter) (Figure 6D2). In contrast, WIVs of the circular cylinder were ≈20%–50% smaller than its VIVs (Figure 6D1), indicating that noise drowned out the signal in the absence of undulations. Furthermore, the dominant frequency of the WIVs decreased with the increasing upstream–downstream separation (Figure 6D2). The results indicated that the seal whisker-inspired sensing structure showed great promise for long-distance wake sensing compared to the smooth cylinder without undulations. The presence of such whisker-inspired sensors in underwater robots can contribute to better trail tracking performance, especially in turbid conditions, much like the seal itself.

We also conducted COMSOL Multiphysics-based simulations to visualize the flow vorticity distributions, thus proposing a mechanistic explanation of the different WIV responses of the seal whisker structure and circular cylinder from the view of the downstream flow vorticity distribution. Specifically, the flow vorticity behind one isolated seal whisker (characterized by one elliptical cross-section, Figure 6E1) showed a smaller distribution area and fluctuations than one isolated circular cylinder (characterized by one circular circle, Figure 6E2), causing the smaller VIV of an isolated seal whisker structure than the circular cylinder. However, when located in the wake of an upstream circular, though the seal whisker's vibration reversely interfered in the oncoming wake, the combined vortices of the upstream wake and the self-shed vortices of the downstream seal whisker still had a more considerable distribution area and vorticity intensity than the vortices only shed by one isolate seal whisker (Figure 6F1). Thus the seal whisker vibrated more (because of the wake of the circular cylinder) when located in the wake compared with being isolated in an opening flow. In this case, the vibration of the seal whisker was only induced by its suppressed shedding vortices (Figure 6E1). In contrast, the upstream wake disturbed the alternate vortices shed by the downstream circular cylinder itself (Figure 6F2), which caused the flow vorticity fluctuation and the alternating distribution characteristic of the combined vortices to be suppressed compared to the isolated circular cylinder, resulting in the smaller WIV than VIV of the circular cylinder (Figure 6D1). In a word, compared to combined vortices (in WIV measurements) of the upstream wake and self-shed vortices, single self-shed vortices (in VIV measurements) had weaker vorticity fluctuations and distribution areas, causing a higher WIV than VIV of the seal whisker. In contrast, single self-shed vortices were stronger than combined vortices for the circular cylinder, causing a lower WIV than VIV of the circular cylinder.

It has been a trend to use swarm underwater robots to carry out underwater operations in recent years.[12,13] However, due to the complexity of the underwater operating environment, the sensory-system-based local information interaction among swarm underwater robots is a challenging problem. Although visual and acoustic sensors provide solutions to the information interaction problem mentioned above, their normal functions will be affected in the complex terrain and the dark environment. As a result, seeking an alternative to visual and acoustic sensors is essential and critical. Furthermore, motions of underwater robots can result in hydrodynamic variations, typically characterized as an alternating shedding vortices-formed vortex street (generated by rhythmic fins) or a jet (generated by the propeller). With the movements of the underwater robots, the above vortex street or jet can form a vortex trail (Figure 1D). By sensing the above vortex trail using onboard flow sensors of a focal underwater robot, its adjacent underwater robots can be detected. The seal whisker-inspired flow sensor developed in this article performed excellent wake detection ability by locking into the shedding frequency of the upstream vortices and showing WIVs ('signal') that were ≈2–10× more than VIV ('noise'), thus realizing an ultrasensitive flow sensor with a high SNR. As a result, the designed sensor is an effective alternative to the visual and acoustic sensors for local information interaction for swarm robots in complex terrain and the dark environment. In addition, the practicality of the cantilever sensor in wake detection provided the third way of validating the sensor operation. The current version of the designed cantilever sensor is not waterproof, since the graphene nanoplatelets sensor is exposed to water. In future work, an insulating layer (e.g., silicone gel or polydimethysiloxane 'PDMS') will be used to seal the graphene and allow sensor operation underwater. In this way, the sensor shows great promise to serve as an efficient seal whisker-inspired wake detector for the future applications in underwater robots.

3. Summary and Future Work

In this article, we developed and employed a bioinspired fully 3D-printed MEMS cantilever sensor, which featured both real and 3D-printed seal whiskers. A high gauge factor graphene nanoplatelets piezoresistor formed at the proximal end of the MEMS cantilever recorded the vibration frequencies and amplitudes of the whisker structure attached at the distal tip of the cantilever. The MEMS whisker sensor was tested in various experimental conditions which mimic the seal whisker's natural active hunting conditions to further explain the ultrasensitive fish wake-tracking capability of the undulating seal whiskers. First, the MEMS sensors were used to measure the natural frequencies of excised harbor (*Phoca vitulina*) and grey (*Halichoerus grypus*) seal whiskers. The MEMS sensor measurements were cross-verified using an LDV measurement and through simulations, which also provided insights into the higher vibration modes of the whiskers. Compared with previous experiments based on the laser doppler vibrometer (LDV) system[46] and particle image velocimetry system,[59] which consisted of complicated setups, the 3D-printed MEMS sensor showed identical experimental efficiency at a low cost. The whisker-inspired MEMS sensors were tested in a recirculating water flume to understand the possible natural orientations of the seal whisker during active hunting, which are deemed beneficial in terms of reduced VIV and drag force. Finally, the 3D printed whisker-inspired MEMS sensors were tested in steady water flows behind a wake generator to study the behavior of frequency locking with the wake frequency even at large distances away from the wake generator and the efficacy of doing so as compared to regular cylindrical structures. The key findings of our work are summarized as below:

Natural Frequency Measurements of Seal Whiskers: The natural frequencies measured by the sensor were 43 ± 4 Hz for grey seal whiskers and ≈27 ± 4 Hz for harbor seal whiskers. Furthermore, LDV-based measurements revealed that natural frequencies of grey and harbor seal whiskers were 64 ± 6 and 33 ± 5 Hz, respectively. In addition, COMSOL Multiphysics-based FEM simulations revealed the five modes of natural frequencies (harbor seal whiskers ≈28–600 Hz, grey seal whiskers ≈20–294 Hz) under the water, providing a reference database of the detectable frequency range of the seal whisker.

VIV Responses of Seal Whisker Structure at Various AOA: The vorticity magnitude fluctuations and the distribution area of shedding vortices showed an increasing trend when the AOA of the seal whisker increased from 0° or 180° (major radius paralleling the flow) to 90° (minor radius paralleling the flow), causing the same trend of the VIV with the AOA. The smallest VIV at the AOA = 0° orientation suggested that the major radius of the seal whisker is parallel to the flow when swimming, ensuring the smallest VIV-induced noise and thus realizing the ultrasensitive sensing of the underwater disturbances. Furthermore, the AOA = 0°–30° or 150°–180° orientation was a limited angle range of VIV suppression of the undulating seal whisker, agreeing with similar studies in the literature performed using time-resolved particle vibrometer measurements.[59]

Long-Distance Wake Detection of the Seal Whisker-Inspired Sensor: The WIVs of the seal whisker structure were 2–10× more than its VIV, while WIVs of the circular cylinder were ≈2–5× smaller than its VIVs. Besides, the WIVs of the seal whisker and the circular cylinder decreased with the increasing separations from the upstream vortex generator because of the decreasing flow vorticity fluctuations and distributions. In addition, the vibration frequency of the whisker-inspired sensor locked efficiently to the vortex-shedding frequency (≈2.75 Hz) of the upstream circular cylinder for a considerable upstream–downstream separation (2.5–10× the whisker diameter), indicating efficient long-distance wake sensing similar to the seal whisker. In contrast, the dominant frequency of the WIVs of the circular cylinder decreased with the increasing upstream–downstream separation. The WIV response of the seal whisker structure revealed that the sensor could detect distant wakes without the signal interfering with self-induced noise. The developed 3D printed MEMS sensor is the first of its kind to demonstrate the whisker-inspired wake tracking ability, and the low form factor of the sensor brings in a high potential for applications of underwater robots (Figure 1D) to assist in environment perception and long-distance object tracking.

In the future, we plan to develop inkjet-printed biocompatible and tattooable piezoresistive sensors which could be mounted directly on real seal whiskers of live seals to record vibrations of seal whiskers as the seal is actively swimming and tracking a fish trail. The frequency components measured by the sensors will then be compared to the fish wake frequencies and the natural frequencies measured and simulated in this article. This will enable us to further investigate the biological mechanisms employed by the seals in interpreting the frequency information sensed by the seal whiskers. In addition, we also plan to develop and test arrays of the MEMS seal whisker-inspired sensors on swarm underwater robots to detect hydrodynamic stimuli generated by the neighboring robots.[61,62]

4. Experimental Section

Scanned Seal Whiskers and Constructed Seal Whiskers: Seal whiskers (five each, Figure 1E) were collected from deceased harbor (*Phoca vitulina*, age ≈10 days to 1–2 years) and grey (*Halichoerus grypus*, adults) seals at the Zeehondencentrum in Pieterburen (the Netherlands). The excised harbor seal whiskers had a larger average length (86.9 ± 9.43 mm, Figure 1E and Table 1) and average thickness (0.4147 ± 0.0261 mm) compared to the grey seal whiskers (length ≈70 ± 3.39 mm, thickness ≈0.3987 ± 0.0166 mm, Figure 1E and Table 1), which were measured using blue light scanning technology (Scanner: GOM ATOS III Triple Scan 8 M). The LDV and MEMS sensor-based natural frequency measurements were conducted on these excised seal whiskers.

In the sensor-based VIV and WIV measurements, a harbor seal whisker structure (Figure 1F) constructed following the geometrical model proposed by Hanke et al. was used,[27] which described the seal whisker's morphology using seven parameters, including α, β, s, t, k, l, and M, explained as follows. The seal whisker had one leading edge and one trailing edge (viewing the seal whisker from a view perpendicular to the paper, Figure 1F), containing peaks and troughs along the whisker length. The oblique cross-section between a peak of the trailing edge and the adjacent peak of the leading edge formed an ellipse (major radius – s, minor radius – t) with an angle α to the whisker axis. The oblique cross-section between a trough of the trailing edge and the adjacent trough of the leading edge formed an ellipse (major radius – k, minor radius – l) with an angle β to the whisker axis. Finally, the distance between the above two oblique cross-sections was defined as M, which is half the wavelength of the undulation of the seal whisker.

The measured values of α, β, s, t, k, l, and M were 3.23 ± 13.47°, 5.07 ± 25.19°, 0.58 ± 0.05 mm, 0.25 ± 0.08 mm, 0.47 ± 0.09 mm, 0.3 ± 0.09 mm, and 1.72 ± 0.2 mm, respectively.[32] One seal whisker was first constructed (15 mm long, with 4.5 troughs along the leading edge) and was then scaled up ten times. The scaled-up seal whisker structure (150 mm long) was 3D-printed using stereolithography (Formlabs Form 3) using the 'Grey Pro' material (flexural modulus ≈2.2 GPa).

3D-Printed Piezoresistive MEMS Cantilever Sensors: The cantilever sensors used in natural frequency and WIV/VIV measurements had similar designs. However, they varied in the dimensions of the cantilever structure, the supporting part, and serpentine grooves due to the design requirements in attaining the desired sensitivity required for the measurements on real-scale and scaled-up whiskers. The designed sensor[63] for the natural frequency measurements had a length of ≈57.5 mm and a width of ≈20 mm (Figure 2A). The sensor was composed of a 3D printed MEMS cantilever structure (length ≈14.5 mm, width ≈10 mm, aspect ratio ≈50, thickness ≈0.3 mm) and a supporting part (length ≈ 20 mm, Figure 2B), both printed using the 'Clear Resin' material (flexural modulus ≈2.2 GPa) of the Formlabs Form 3 3D printer. In order to realize the graphene nanoplatelets (commercially obtained from Graphene Supermarket, average nanoplatelet thickness ≈7 µm) piezoresistive sensing elements, drop-casting was performed wherein dilute conductive graphene nanoplatelets dispersion (1:4 volume dilution in ethanol) was dropped into serpentine-shaped grooves (depth ≈100 µm, Figure 2C) situated at the anchor of the cantilever structure. Graphene nanoplatelets (Figure 2D) were preferred due to the high gage factor,[64] which rendered high sensitivity to the MEMS cantilever sensor. The seal whiskers were embedded into a hole on the MEMS cantilever's distal end (Figure 2C). They were sealed using a soft polymer (Elastic resin, Formlabs, tensile modulus ≈3 MPa) which mimicked the soft FSC holding[43] as is the case in biological whiskers. In the experiments, the sensor's supporting fixture (length ≈20 mm) was attached to a rigid holder (Figure 2E). By manually plucking the whisker along the overall minor axis of the seal whisker (Video S1, Supporting Information), the freely-vibrating cantilever sensor's piezoresistive outputs (sampling frequency ≈5 kHz) were recorded via a Wheatstone bridge circuit (Figure 2E). FFT analyses were conducted on the recorded sensor outputs, and the dominant peaks in the frequency domain were noted, which indicated the natural frequencies of the seal whiskers.

The sensor (length 50 mm, width 35 mm, Figure 2F1–3) used in WIV and VIV measurements was 3D-printed using the 'Grey Pro' material of Formlabs Form 3. To ensure that the sensor is sufficiently sensitive to the tiny vibrations of the seal whisker structure attached at the end of the sensor, the cantilever structure was designed to be longer (25 mm long, Figure 2F3) and thinner (thickness 0.5 mm, Figure 2F3) than the sensor used in natural frequency measurements. Besides, considering that the resistance variations of the graphene piezoresistor were mainly caused by the strain variations at the root of the cantilever,[65] the serpentine grooves (length 5 mm, Figure 2F3) were shortened to ensure that the sensor was more sensitive to the tiny vibrations of the seal whisker structure. Finally, the 3D-printed seal whisker structure was inserted into a 3D-printed whisker holder and attached to the distal end of the MEMS sensor.

The LDV System: The LDV system[66] used in this work consisted of a laser sensor (OFV-534 Compact Sensor Head) and a velocity and displacement decoder (OFV-5000 Vibrometer Controller) from Polytec Company (Figure 3A). The OFV-5000 controller decoded the velocity and displacement signals from the OFV-534 compact sensor head in real-time, enabling accuracy in the picometer range using the small laser spot from the sensor head. The sensor head was equipped with a manual focus and an integrated optical signal level indicator, both optimized prior to the measurements to ensure the best signal output quality. The seal whisker was mounted on a 3D-printed holder (depth ≈10 mm) with the soft encapsulation of the whisker base (Elastic resin, Formlabs Company) that resembled the soft follicle-sinus complex (FSC)[43] embedded in the seal muzzle.

The seal whisker was oriented with its overall minor axis parallel to the laser. In addition, the printed holder with the seal whisker was mounted on a rigid holder. By plucking the seal whisker manually along the whisker's minor axis, the laser beam from the sensor head was reflected by the timely displacement (x(t), Figure 3B) of the vibrating seal whisker. As a result, the laser frequency shifted proportionally to the seal whisker's vibrating velocity (v(t), Figure 3B). Furthermore, the vibration velocity was independent of the reflected laser intensity. Hence the measurement still had high accuracy when the seal whisker had low reflectivity. A high-precision interferometer and digital decoding electronics in the velocity and displacement decoder (OFV-5000 Vibrometer Controller) transformed the frequency shift into a voltage signal subsequently collected by the DAQ data acquisition system. By conducting an FFT analysis on the collected voltage, natural frequencies of the seal whiskers were determined by noting the first dominant peak in the frequency domain.

Finite Element Simulations of Natural Frequency: COMSOL Multiphysics software[67] was used to simulate the natural frequencies: of 1) an isolated seal whisker in the air (Figure 4A), 2) the seal whisker mounted on a cantilever sensor (Figure 4B--F), and 3) an isolated seal whisker under the water (Figure 4G). In case 1, the whisker base was rigidly fixed to simulate the LDV-based measurements, and case 2 simulated the cantilever sensor-based measurements. In case 3, five modes of underwater natural frequencies were collected to compare with the in-air natural frequencies calculated in case 1. In the simulations, Young's modulus, density, and Poisson's ratio of the seal whisker used were 6 GPa, 1300 kg m^{-3}, and 0.4, respectively. The material properties mentioned above were determined through nanoindentation tests[68] and Archimedes' principle experiments conducted on the excised seal whiskers. The 3D printed cantilever structure had a Young's modulus of 2.8 GPa, a Poisson's ratio of 0.41, and a density of 1200 kg m^{-3}. The Young's modulus, density, and Poisson's ratio of the soft polymer (Elastic resin, Formlabs) were 3.2E6 Pa, 0.41, 1200 kg m^{-3}, respectively.

In case 1, the seal whisker was embedded into a soft cylindrical base (diameter 20 mm, height 10 mm, Figure 4A) with fixed walls and a fixed bottom. A free tetrahedral mesh with a minimum element size of 8.99×10^{-5} m and a maximum element size of 2.1×10^{-3} m was used to guarantee that the seal whisker's 3D geometry stayed unscathed after the meshing operation (Figure 4A). In case 2, a free tetrahedral mesh with a minimum element size of 1.01×10^{-4} m and a maximum element size of 2.35×10^{-3} m was applied to the sensor and the seal whisker (Figure 4B). In case 3, a cylindrical water domain (diameter 0.2 m, height 0.1 m, Figure 4F) surrounded the isolated seal whisker with the soft base. A minimum element size of 3.06×10^{-4} m and a maximum element size of 7.13×10^{-3} m were defined for the calculated domains. The number of elements in the mesh was $\approx 10^5$.

In cases 1 and 2, a direct MUMPS solver simulated mode shapes and natural frequencies of the seal whisker and cantilever sensor. In addition, the natural frequency in the first mode shape (Figure 4D,E) was collected to compare with the measured natural frequency for the seal whisker. In case 3, a fully-coupled acoustics (water domain) – structure (seal whisker) study was simulated using the MUMPS solver for the simulated models.

VIV and WIV Measurements: VIVs and WIVs of the seal whisker and the circular cylinder (of similar dimensions as the seal whisker) were measured and compared. A circular cylinder of diameter 8 mm (average value of major and minor radii of the seal whisker), 3D-printed using the same material, was used to guarantee comparability of the WIVs and VIVs of the seal whisker and the circular cylinder. The VIVs and WIVs mentioned were characterized through dominant peaks in the frequency domain obtained from FFT analyses on time series of sensor outputs. In the flow experiments, the printed cantilever sensor was located in the test section of the recirculating water flume (5L Loligo System swim tunnel, Figure 3C) above the surface of the water, with the seal whisker or the circular cylinder immersed into water (depth ≈8 cm). In the VIV measurement experiments, the seal whisker was located with a specific AOA to the flow (velocity 0.15 m s^{-1}). The AOA varied from 0 to 180°, with an interval of 15°. The AOA of 90° and 0° meant that the overall minor radius (0°) and major (90°) radius of the seal whisker were parallel with the oncoming flow, respectively (Figure 3D). In the WIV measurements,

a circular cylinder was located upstream with a 20–80 mm separation from the downstream circular cylinder or seal whisker (Figure 3E). The downstream seal whisker was located with its overall major axis parallel to the oncoming flow (0.1 m s^{-1}) in WIV experiments.

Supporting Information

Supporting Information is available from the Wiley Online Library or from the author.

Acknowledgements

The authors acknowledge Nitesh Anerao for helping to set up the LDV measurements. Besides, they express their sincere gratitude to the Zeehondencentrum (Pieterburen, the Netherlands), especially Ana Rubio Garcia, Sander van Dijk, Anna Salazar Casals, and Margarita Méndez Aróstegui, for providing them with harbor and grey seal whiskers and assisting them during whisker excision. In addition, A.G.P.K. gratefully acknowledges funding from the University of Groningen's start-up grant and the European Research Council (grant no. ERC-STG-101042370). Finally, M.C. gratefully acknowledges funding from the European Research Council (grant no. ERC-CoG-771687). The flow velocity in Section 2.2 was corrected to 0.15 ms^{-1} on November 17, 2022 after initial online publication.

Conflict of Interest

The authors declare no conflict of interest.

Authors Contribution

X.Z., A.K., A.O.K., M.C., and A.G.P.K. performed conceptualization. X.Z. performed Methodology. X.Z. performed investigation. X.Z. performed visualization. A.O.K., M.C., and A.G.P.K. performed supervision. X.Z. wrote the original draft. X.Z., A.K., A.O.K., M.C., and A.G.P.K. reviewed and edited the final manuscript.

Data Availability Statement

The data that support the findings of this study are available from the corresponding author upon reasonable request.

Keywords

3D printing, seal whiskers, underwater sensing, vortex-induced vibrations, wake-induced vibrations

Received: June 26, 2022
Revised: July 28, 2022
Published online: August 26, 2022

[1] G. Antonelli, in *Encyclopedia of Systems and Control*, Springer International Publishing, Cham **2021**.
[2] R. D. Christ, R. L. WernliSr, *The ROV manual: a user guide for remotely operated vehicles*, Butterworth-Heinemann, Oxford **2013**.
[3] G. Griffiths, *Technology and applications of autonomous underwater vehicles*, CRC Press, Boca Raton, USA **2022**.
[4] L. Lin, H. Xie, D. Zhang, L. Shen, *J. Bionic Eng.* **2010**, *7*, 177.
[5] R. Salazar, V. Fuentes, A. Abdelkefi, *Ocean Eng.* **2018**, *148*, 75.
[6] Y. S. Ryuh, G. H. Yang, J. Liu, H. Hu, *J. Bionic Eng.* **2015**, *12*, 37.
[7] J. E. Chang, S. W. Huang, J. H. Guo, in *IEEE/OES Autonomous Underwater Vehicles (AUV)*, **2016**, 49.
[8] O. Khatib, X. Yeh, G. Brantner, B. Soe, B. Kim, S. Ganguly, H. Stuart, S. Wang, M. Cutkosky, A. Edsinger, P. Mullins, *IEEE Robot Autom. Mag.* **2016**, *23*, 20.
[9] S. W. Huang, E. Chen, J. Guo, *IEEE J. Oceanic Eng.* **2017**, *43*, 7.
[10] Z. Wu, J. Liu, J. Yu, H. Fang, *IEEE/ASME T. Mech.* **2017**, *22*, 2130.
[11] A. Vasilijević, Đ. Nađ, F. Mandić, N. Mišković, Z. Vukić, *IEEE/ASME T. Mech.* **2017**, *22*, 1174.
[12] J. S. Jaffe, P. J. Franks, P. L. Roberts, D. Mirza, C. Schurgers, R. Kastner, A. Boch, *Nat. Commun.* **2017**, *8*, 14189.
[13] R. dell'Erba, *Contin. Mech. Thermodyn.* **2020**, https://doi.org/10.1007/s00161-020-00923-y.
[14] J. Montgomery, S. Coombs, M. Halstead, *Rev. Fish Biol. Fish.* **1995**, *5*, 399.
[15] H. W. Lissmann, K. E. Machin, *J. Exp. Biol.* **1958**, *35*, 451.
[16] R. Krahe, E. S. Fortune, *J. Exp. Biol.* **2013**, *216*, 2363.
[17] J. R. Solberg, K. M. Lynch, M. A. MacIver, *Int. J. Robot. Res.* **2008**, *27*, 529.
[18] A. T. Abdulsadda, X. Tan, *Bioinspir. Biomim.* **2013**, *8*, 026005.
[19] Y. Bai, J. B. Snyder, M. Peshkin, M. A. MacIver, *Int. J. Robot. Res.* **2015**, *34*, 1255.
[20] R. Bouffanais, G. D. Weymouth, D. K. Yue, *Proc. R. Soc. A: Math. Phys. Eng. Sci.* **2011**, *467*, 19.
[21] C. Chevallereau, M. R. Benachenhou, V. Lebastard, F. Boyer, *IEEE Trans. Robot.* **2014**, *30*, 604.
[22] J. Zheng, X. Zheng, T. Zhang, M. Xiong, G. Xie, *Bioinspir. Biomim.* **2020**, *15*, 046003.
[23] G. Dehnhardt, B. Mauck, H. Bleckmann, *Nature* **1998**, *394*, 235.
[24] G. Dehnhardt, B. Mauck, W. Hanke, H. Bleckmann, *Science* **2001**, *293*, 102.
[25] X. Zheng, A. M. Kamat, M. Cao, A. G. P. Kottapalli, *J. R. Soc. Interface* **2021**, *18*, 20210629.
[26] R. D. Gabbai, H. Benaroya, *J. Sound Vib.* **2005**, *282*, 575.
[27] W. Hanke, M. Witte, L. Miersch, M. Brede, J. Oeffnet, M. Michael, F. Hanke, A. Leder, G. Dehnhardt, *J. Exp. Biol.* **2010**, *213*, 2665.
[28] H. R. Beem, M. S. Triantafyllou, *J. Fluid Mech.* **2015**, *783*, 306.
[29] G. Weymouth, M. Triantafyllou, *APS Division of Fluid Dynamics Meeting Abstracts* **2011**, *64*, S27.
[30] A. W. Rinehart, W. Zhang, V. Shyam, in 55th AIAA Aerospace Sciences Meeting, Grapevine, USA, 2017.
[31] X. Zhang, X. Shan, T. Xie, J. Miao, H. Du, R. Song, *Measurement* **2021**, *172*, 108866.
[32] X. Zheng, A. M. Kamat, V. S. Harish, M. Cao, A. G. P. Kottapalli, in 21st Int. Conf. Solid-State Sensors, Actuators and Microsystems (Transducers), **2021**, 1271.
[33] J. Z. Gul, K. Y. Su, K. H. Choi, *Soft Robot* **2018**, *5*, 122.
[34] P. V. Alvarado, V. Subramaniam, M. Triantafyllou, in *IEEE Int. Conf. Intell. Robots Syst.*, Tokyo, **2013**.
[35] A. G. P. Kottapalli, M. Asadnia, H. Hans, J. M. Miao, M. S. Triantafyllou, in *IEEE 27th Int. Conf. Micro Electro Mech. Syst.*, San Francisco, USA, **2014**.
[36] A. G. P. Kottapalli, M. Asadnia, J. M. Miao, M. S. Triantafyllou, in *28th IEEE Int. Conf. Micro Electro Mech. Syst.*, Estoril, Portugal, **2015**.
[37] H. Beem, M. Hildner, M. Triantafyllou, *Smart Mater. Struct.* **2012**, *22*, 014012.
[38] P. Xu, X. Wang, S. Wang, T. Chen, J. Liu, J. Zheng, W. Li, M. Xu, J. Tao, G. Xie, *Research* **2021**, 9864967.
[39] M. Xu, S. Wang, P. Xu, X. Wang, J. Zheng, X. Liu, T. Chen, H. Wang, G. Xie, J. Tao, J. Liu, Underwater Bionic Whisker Sensor Based on Triboelectric Nanogenerator for Passive Vortex Perception. Available at SSRN 4023037.

[40] H. Beem, *Ocean. Mag.* **2016**, *51*, 82.
[41] The Economist, https://www.economist.com/science-and-technology/2018/08/09/seals-whiskers-provide-a-model-for-the-latest-submarine-detectors, **2018**.
[42] V. Shyam, A. Ameri, P. Poinsatte, D. Thurman, A. Wroblewski, C. Snyder, in ASME Turbo Expo 2015: Turbine Technical Conference and Exposition, Montreal **2015**.
[43] A. Jones, C. D. Marshall, *Anat. Rec.* **2019**, *302*, 1837.
[44] C. D. Marshall, H. Amin, K. M. Kovacs, C. Lydersen, *Anat Rec.* **2006**, *288*, 13.
[45] K. A. Mcgovern, C. D. Marshall, R. W. Davis, *Anat. Rec.* **2015**, *298*, 750.
[46] C. T. Murphy, W. C. Eberhardt, B. H. Calhoun, K. A. Mann, D. A. Mann, *PLoS One* **2013**, *8*, e69872.
[47] W. C. Young, R. Budynas, *Roark's Formulas for Stress and Strain. Seventh*, McGraw-Hill Professional Publishing, New York **2001**.
[48] H. Hans, J. M. Miao, M. S. Triantafyllou, *Bioinspir. Biomim.* **2014**, *9*, 036013.
[49] L. F. Shatz, T. De Groot, *PLoS One* **2013**, *8*, e54876.
[50] H. Bleckmann, T. Breithaupt, R. Blickhan, J. Tautz, *J. Comp. Physiol. A* **1991**, *168*, 749.
[51] K. Lyons, C. T. Murphy, J. A. Franck, *PLoS One* **2020**, *15*, e0241142.
[52] C. T. Murphy, C. Reichmuth, W. C. Eberhardt, B. H. Calhoun, D. A. Mann, *Sci. Rep.* **2017**, *7*, 8350.
[53] D. Renouf, *J. Zool.* **1979**, *188*, 443.
[54] M. Muthuramalingam, C. Brnuecker, *Sci. Rep.* **2019**, *9*, 12808.
[55] G. Liu, Q. Xue, X. Zheng, in APS Division of Fluid Dynamics Meeting Abstracts, C27-006 **2019**.
[56] S. Weigert, M. Dreier, M. Hegner, *Appl. Phys. Lett.* **1996**, *69*, 2834.
[57] L. Miersch, W. Hanke, S. Wieskotten, F. D. Hanke, J. Oeffner, A. Leder, M. Brede, M. Witte, G. Dehnhardt, *Philos. Trans. R. Soc. Lond., B, Biol. Sci.* **2011**, *366*, 3077.
[58] R. W. Dykes, *J. Neurophysiol.* **1975**, *38*, 650.
[59] S. Wang, Y. Liu, *Exp. Fluids* **2016**, *57*, 32.
[60] T. Wei, W. W. Willmarth, *J. Fluid Mech.* **1989**, *204*, 57.
[61] X. Zheng, C. Wang, R. Fan, G. Xie, *Bioinspir. Biomim.* **2017**, *13*, 016002.
[62] X. Zheng, W. Wang, L. Li, G. Xie, *Bioinspir. Biomim.* **2020**, *16*, 016012.
[63] X. Zheng, A. M. Kamat, M. Cao, A. G. P. Kottapalli, in *The 35th Int. Conf. Micro Electro Mech. Syst.*, Tokyo, **2022**.
[64] A. M. Kamat, Y. Pei, B. Jayawardhana, A. G. P. Kottapalli, *ACS Appl. Mater. Interfaces* **2021**, *13*, 1094.
[65] A. M. Kamat, X. Zheng, B. Jayawardhana, A. G. P. Kottapalli, *Nanotechnology* **2020**, *32*, 095501.
[66] H. H. Nassif, M. Gindy, J. Davis, *Ndt E Int* **2005**, *38*, 213.
[67] C. O. Multiphysics, *COMSOL Multiphysics*, Burlington, MA, (accessed: July 2018).
[68] C. A. Schuh, *Mater. Today.* **2006**, *9*, 32.